IVYSPRING INTERNATIONAL PUBLISHER

Theranostics

2017; 7(7): 1781-1794. doi: 10.7150/thno.18437

Research Paper

Dual-Responsive Molecular Probe for Tumor Targeted Imaging and Photodynamic Therapy

Xiaoqing Meng[1, 2*], Yueting Yang[1*], Lihua Zhou[1, 3], li Zhang[1], Yalin Lv[1], Sanpeng Li[1, 2], Yayun Wu[1], Mingbin Zheng[1,4,5], Wenjun Li[1], Guanhui Gao[1], Guanjun Deng[1,2], Tao Jiang[1] , Dapeng Ni[1, 2], Ping Gong[1, 4, 5]✉ and Lintao Cai[1]✉

1. Guangdong Key Laboratory of Nanomedicine, CAS Key Lab of Health Informatics, Shenzhen Institutes of Advanced Technology, Chinese Academy of Sciences, Shenzhen 518055, China;
2. University of Chinese Academy of Sciences, Beijing 100049, China;
3. College of Life Sciences, Hunan Normal University, Changsha 410081, China;
4. Guangdong Key Laboratory for Research and Development of Natural Drugs, Guangdong Medical University, Dongguan 523808, China;
5. State Key Laboratory of Chemo/Biosensing and Chemometrics, Hunan University, Changsha 410082, China.

*Equal contribution

✉ Corresponding authors: Ping Gong, E-mail: ping.gong@siat.ac.cn; Tel: +86 755 8639 2223. Lintao Cai, E-mail: lt.cai@siat.ac.cn; Tel: +86 755 8639 2210.

Received: 2016.11.21; Accepted: 2017.02.08; Published: 2017.04.10

Abstract

The precision oncology significantly relies on the development of multifunctional agents to integrate tumor targeting, imaging and therapeutics. In this study, a first small-molecule theranostic probe, RhoSSCy is constructed by conjugating 5′-carboxyrhodamines (Rho) and heptamethine cyanine IR765 (Cy) using a reducible disulfide linker and pH tunable amino-group to realize thiols/pH dual sensing. *In vitro* experiments verify that RhoSSCy is highly sensitive for quantitative analysis and imaging intracellular pH gradient and biothiols. Furthermore, RhoSSCy shows superb tumor targeted dual-modal imaging via near-infrared fluorescence (NIRF) and photoacoustic (PA). Importantly, RhoSSCy also induces strongly reactive oxygen species for tumor photodynamic therapy (PDT) with robust antitumor activity both *in vitro* and *in vivo*. Such versatile small-molecule theranostic probe may be promising for tumor targeted imaging and precision therapy.

Key words: Small-molecule theranostic probe, Dual-stimuli sensing, NIRF/PA imaging, tumor targeting, Photodynamic therapy.

Introduction

As cancer is proliferating fast, the innovated diagnostic and therapeutic strategies are imperative for early detection and precision treatment. The emergence of theranostics, known as new concept for integrated diagnostics and therapeutics in a single system [1, 2], provides good strategies to monitor response to treatment real-timely, as well as to optimize the efficacy and safety of therapy for potentially transformative advances in biomedicine [3, 4]. Theranostics seems to streamline the entire drug development process and results in significant cost savings for the overall healthcare system [5]. Therefore, theranostic probes integrating diagnostic imaging and therapeutic functions in a single system are emerging as alternatives to independently administered diagnostic contrast agents and traditional cancer therapy strategies [6, 7].

Nanoparticle-based theranostic probes now become a fascinating tool and hot topic of research due to their ultrahigh capacity to ferry cargo with various agents and drugs into them [8, 9]. The theranostic nanoprobes provide several potential advantages, including extension of circulating half-life, passive accumulation at tumor sites due to the enhanced permeability and retention (EPR) effect, active targeting of tumor cells, reduced toxicity, and integration of multiple imaging and treatment functions in a single complex [10-17]. However, there

still are scientific and industrial challenges for developing nanoparticle-based theranostic nanoprobes for clinical application [18], such as the complexity and uncontrollability of nanoparticles, unstability in the blood, unavoidable non-specific uptake by reticular epithelial system (RES) [19, 20], the difficulties in large-scale preparation with good repeatability and uncertain nanomaterial toxicity [21-25]. Particularly, the targeting efficiency of nanoparticle-based delivery vehicles is far below desired [26, 27].

It is valuable to reconsider the small molecule probes, which are simple in structure and easy to synthesize and control, could address the dilemma of nanomaterials. Recently, several multifunctional small molecule dyes have been identified for specific targeting and imaging of interested tissues [28-30]. Cancer-selective nearinfrared (NIR) fluorescent heptamethine indocyanine dyes are shown to preferentially accumulate in tumor cells and function in the `wavelength range of 700-900 nm in which the intrinsic chromophores in native tissue are extremely low to visualize tumors in vivo sensitively and noninvasively. This dye also shows photodependent cytotoxic activity, suggesting a potential theranostic agent for tumor targeting, imaging and photodynamic therapy (PDT) [31, 32]. These structure-inherent near-infrared fluorophores can be used for tumor theranostics and image-guided surgery [6, 33-40]. However, it is still high challengeable for small-molecule theranostic probe to achieve so many functions including target, multi-modal imaging and therapy.

In addition, amino acids containing the thiol groups are components of many peptides that play crucial roles in maintaining biological redox homeostasis in biological systems through an equilibrium between reduced free thiol and oxidized disulfide forms [41]. Importantly, numerous investigations have demonstrated that abnormal levels of these amino acids are closely associated with certain disease states, including liver damage, cancer, AIDS, osteoporosis, Alzheimer's disease, and heart, inflammatory bowel, and cardiovascular diseases [42-50]. It was observed that the oxides of cysteine in protein were more prevalent in tumor tissues taken from patients, relative to matched normal tissues. The redox imbalance thus may be related to oncogenic stimulation. Moreover, oxidative stress has great significance in tumorigenesis and may potentiate HER2-subtype breast tumor spread [51-53]. Consequently, assessments of the levels of thiol-containing substances in biological systems may aid early diagnosis of some diseases.

Herein, we reported a first small-molecule theranostic probe with "Four in One" functions including thiols/pH sensing, tumor targeting, NIRF/PA dual-modal imaging and PDT therapy. RhoSSCy was synthesized by conjugating Rho with Cy via a disulfide linker and pH tunable amino-group, which allowed probe to respond to both thiols and pH in tumor microenvironments. At the same time, the probe not only exhibited intrinsic preferential tumor accumulation, but also performed NIRF/PA dual-modal imaging and photosensitizing antitumor activities with photodynamic therapy. Therefore, the well-defined RhoSSCy as a dual-responsive small-molecule probe and theranostic agent may have important implications for tumor targeted imaging and precision therapy.

Experimental Procedures

Materials

N,N-Dimethylformamide (DMF), dichloromethane, dicyclohexylcarbodiimide (DCC), 4-dimethylaminopyridine (DMAP), 2',7'-Dichlorofluorescein diacetate (DCFH) and other chemical reagents were purchased from J&K Scientific. DMEM medium, fetal bovine serum (FBS) and kanamycin sulfate were purchased from Invitrogen Co. Ltd. All reagents were purchased from commercial suppliers and used without further purification. Solvents used were purified by standard methods prior to use. MCF-7, A549 and 293-T cells were kindly provided by the Cell Center of our institute. The buffer solutions were as follows: the high K^+ buffer buffer containing 30 mM NaCl, 120 mM KCl, 1 mM $CaCl_2$, 0.5 mM $MgSO_4$, 1 mM NaH_2PO_4, 5 mM glucose, 20 mM HEPES (various pH values were adjusted by NaOH); phosphate buffered saline solution (PBS) containing 137 mM NaCl, 2.7 mM KCl, 4.3 mM Na_2HPO_4, 1.4 mM KH_2PO_4 (pH 7.4). ^1H NMR spectra were recorded on CD_3OD solutions using a Bruker AM-400 spectrometer. Mass spectra were obtained using a JMS-HX 110A/110A Tandem Mass Spectrometer (JEOL). UV-Vis spectra were obtained using a Scinco 3000 spectrophotometer (1 cm quartz cell) at 25 °C. Fluorescence spectra were recorded on FSP920 spectrofluorometer (Edinburgh Instruments, the UK)). Deionized water was used to prepare all aqueous solutions.

Synthesis of Cy-cytamine

2-[4-Chloro-7-(1-ethyl-3,3-dimethyl(indolin-2-ylidene)]-3,5-(propane-1,3-diyl)-1,3 ,5-heptatrien-1-yl)-1-ethyl-3,3-dimethyl-3H-indolium (Cy.7.Cl) was synthesized according to the previous synthesis protocols [54]. Then Cy.7.Cl (61 mg, 0.1 mmol) was dissolved in anhydrous DMF (5 mL). Then, cystaminedihydrochloride (225.2 mg, 1.0 mmol) was

added to it immediately at 0 °C and stirred dramatically. The reaction mixture was heated at 30 °C for 5h under Nitrogen atmosphere. Finally, the solvent was evaporated under reduced pressure to give crude products, which was further purified by silica gel column chromatography with the dichloromethane and methanol to afford pure blue product. Yield: 52 mg (69%). The product (Cy-cytamine) was confirmed by mass spectra.

Synthesis of Cy-cytamine-4/5 carboxyl rhodamine (RhoSSCy)

RhoSSCy was synthesized according to the protocols as shown in Scheme 1. Firstly, the mixture of 1a/b was prepared following the method described in the literature [55]. Then the mixture of 1a/b (48.6 mg, 0.1 mmol), DCC (22.7 mg, 0.11 mmol) and DMAP (6.1 mg, 0.05 mmol) was added in dry dichloromethane and dramatically stirred until all of the materials was dissolved completely, the process needed about 3h. Next, adding the other material Cy-Cytamine (35 mg, 0.05 mmol) into the mixture. The reaction mixture was heated at 30 °C for 7h under Nitrogen atmosphere. Finally, the solvent was evaporated under reduced pressure to give crude products, which was further purified by silica gel column chromatography with the dichloromethane and methanol to afford pure blue product. Yield: 28 mg (42%). The product was confirmed by mass spectra and ^{1}H NMR.

Fluorescence measurement

The fluorescence spectra were investigated using a FSP920 spectrofluorometer (Edinburgh Instruments, the UK). The excitation and emission monochromator slits were both set to 2 nm, 3 nm, respectively. For the fluorescence emission spectra, the excitation wavelength for RhoSSCy was set to 480 nm and 640 nm, respectively. To measure the variation of fluorescent intensity of RhoSSCy with pH and thiols, the λ_{ex} was set to the same wavelength mentioned above and the emission wavelength (λ_{em}) was set to 576 nm and 765 nm, respectively.

Dichlorofluorescein (DCF) assay

200 μmol DCFH was added to 1 mL RhoSSCy/Ce6 solutions at varied concentrations (0, 20,40,60,80 μM) and Ce6 (0, 20,40,60,80 μM). Then, each solution was located in 1 cm quartz cell and irradiated using 660 nm He-Ne laser (DPSS 660 nm Red Laser, i-Nexus, Inc.). The fluorescence intensity of DCF was measured using spectrophotometer (λ_{ex} at 485 nm, λ_{em} at 520 nm).

Cell culture

Cells were cultured in 1640 medium containing 10% fetal bovine serum (FBS), 100 U/mL penicillin and 100 μg/mL streptomycin in a humidified atmosphere with 5% CO_2 at 37 °C. The cells were maintained in an exponential growth phase by periodic subcultivation. The cell density was determined using a hemocytometer, and this was performed prior to any experiments. MCF-7 cells for imaging were initially seeded in 35 mm glass bottom dishes (P35G-0-10-C, MatTek Corp.) at a density of 200,000 cells/well with medium containing 10 % FBS overnight.

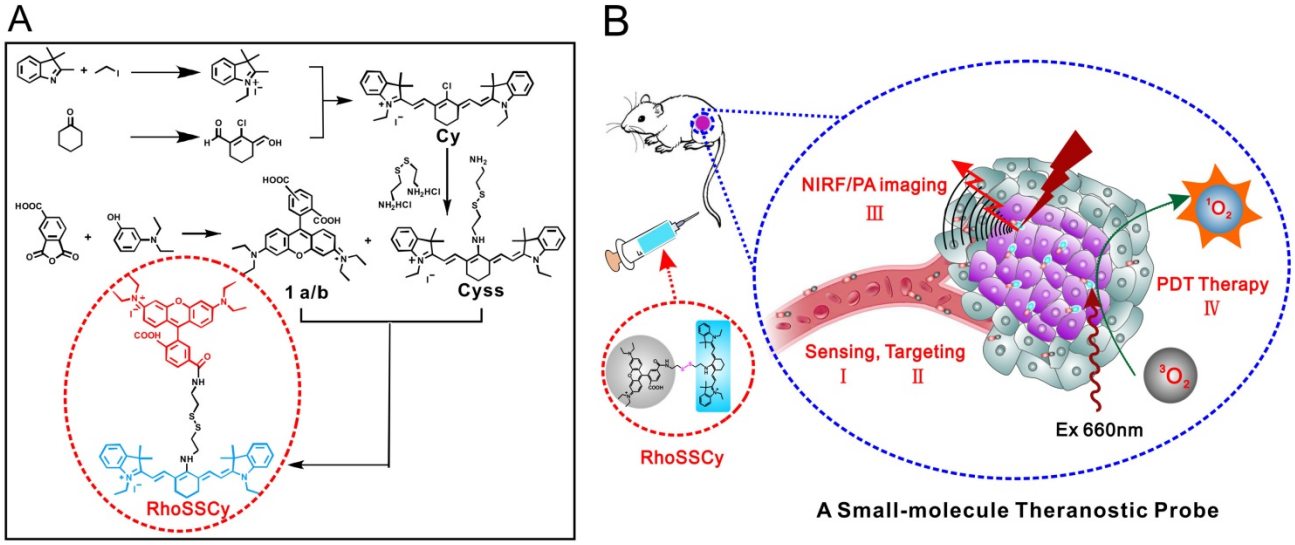

Scheme 1. Illustration of synthesis and functions of RhoSSCy. (A) Synthetic scheme of probe RhoSSCy. (B) Illustration of the theranostic strategy of RhoSSCy.

LSCM fluorescence imaging

To examine the possibility of RhoSSCy for ratiometric imaging applications in living cells, the living MCF-7 cells were washed with PBS for 2 times, incubating for 10 min in the high K^+ buffer buffer solution of different pH values containing nigericin (10 μM), which could homogenize the intracellular pH to that of the incubating buffers and culture medium [56]. And then the cells were further incubated with RhoSSCy (3 μM) at 37 °C for 20 min. By contrast, in the groups without biothiols, the cells were pre-treated with N-ethylmaleimide (NEM, as a thiol-reactive reagent that can block cellular thiols) for 30 min before being incubated with the probe. At last cells were captured by using Laser Scanning Confocal Microscope (LSCM, Leica TCS SP5). Rho channel and Cy channel were excited at 543 nm and 633 nm, respectively, and collected in the ranges of 550-630 nm and 670-800 nm, respectively.

Flow cytometry

Cellular pH response to RhoSSCy was quantified by flow cytometry. Cells were seeded into 6-well plates at a density of 2-5 10^5×cells/well in 2 mL of media and grown in a humidified 5% CO_2 atmosphere at 37 °C for 48 h. Cells were incubated for treated time in 1 ml PBS containing RhoSSCy with different pH value for 15 min at 37 °C. Following the incubation, the cells were washed three times with PBS, gently dissociated from the wells with trypsin, and then resuspended in PBS. Cellular fluorescence was measured on the flow cytometer using 20 mW 633 nm Red JDS Uniphase Helium Neon laser and detector with 780/60 nm emission filter, (BD FACSCanto™ II, BD Biosciences). Infrared channel (APC-Cy7) was used with excitation at 633 nm and collection in the ranges of 750-810 nm.

Cytotoxicity assay

The cytotoxicity of RhoSSCy was evaluated by the Cell Counting Kit-8 (CCK 8, Dojindo, Japan). Briefly, 0.1 ml of MCF-7 cells were seeded in 96 bottom microplates at a density of 7000 cells/well, and incubated with RhoSSCy at varied concentrations (0-80 μM) at 37°C for 24 h. Then, 10 μL CCK-8 solution was added to each well, followed by incubation at 37°C for 4 h. After shaking the plates for 10 min, absorbance values of the wells were read with a microplate reader at 450 nm. The cell viability of treated cells was then obtained by comparison with the incubated but non-exposed control.

Animals and tumor model

50 BALB/c nude mice were provided by Medical Experimental Animal Center of Guangdong Province. They were 4-6 weeks old at the start of each experiment and weighed 20-25 g. For tumor implantation, 30 nude mice received a subcutaneous injection of 5×10^6 MCF-7 cells suspended in 0.2 mL of saline solution in the right hind limb. Tumors were then allowed to grow to 1-2 cm in diameter for 10-30 days. All animal operations were in according with institutional animal use and care regulations, approved by the Laboratory Animal Center of Guangdong.

In vivo fluorescence imaging

Before imaging, the nude mice, with MCF-7 tumors, were anesthetized with an intraperitoneal (IP) injection of 70-100 mg/kg pentobarbital sodium. Once the mice were anesthetized to be motionless, 150 μL 150 μM RhoSSCy was injected via the tail vein. At specified times, dorsal region fluorescence images of of live mice or freshly removed tumor tissues and organs of treated mice were taken by a Maestro™ *in vivo* fluorescence imaging system (Cambridge Research & Instrumentation, Inc. USA). A band pass filter (616-661 nm) and a 675 nm long pass filter were selected to be used as the excitation filter and the emission filter, respectively.

PA imaging

The nude mice with MCF-7 tumors were anesthetized with pentobarbital sodium and 150 μL 150 μM RhoSSCy was injected via the tail vein. For *in vivo* PA imaging, the mice were placed in supine position in the animal holder. Cross-sectional multispectral optoacoustic image datasets were acquired through the tumor at single wavelengths in the NIR window (690 nm) using whole body multispectral optoacoustic tomography (MSOT) system (iThera Medical, Inc. Germany). The raw signals were reconstructed and specific signals were spectrally resolved by the pseudo-inverse unmixing method as implemented in the ViewMSOT software.

In vivo PDT treatment

The mice (six per group) were injected with 150 μL 150 μM RhoSSCy via the tail vein. For laser treatment groups, the tumors of mice were irradiated by the 660 nm laser at 100 mW cm^{-2} for 30 min, and the tumor volume or body weight of the mice was recorded. To further detect the PDT effect *in vivo*, tumors at 48 h after treatment were stained with hematoxylin and eosin. On 30 d, livers and kidneys which had a major accumulation of RhoSSCy were stained with hematoxylin and eosin for biosafety evaluation.

Statistical analysis

Data were reported as mean ±SD. The

differences among groups were determined using one-way ANOVA analysis followed by Tukey's post-test; (*) $P < 0.05$, (**) $P < 0.01$.

Results

Synthesis and characterization of probe RhoSSCy

The small-molecule probe RhoSSCy was synthesized following the strategy shown in Scheme 1A. We got the small-molecule probe RhoSSCy holding a disulfide linker and pH tunable amino-group by the reaction of 1a/b and CySS which were prepared in our lab. The disulfide linker and pH tunable amino-group allowed probe respond to both thiols and pH in tumor microenvironments. At the same time, the probe not only exhibited intrinsic preferential tumor accumulation, but also performed NIRF/PA dual-modal imaging and photosensitizing antitumor activities with photodynamic therapy. As shown in Scheme 1B, RhoSSCy was designed as "Four in One" molecular theranostic probe with multifunctions including thiols/pH dual-response, tumor targeted NIRF/PA dual-modal imaging and PDT.

The structures of these new compounds were confirmed by the mass spectra and ^{1}HNMR (Figure S1, S2 and Figure S3). Since RhoSSCy was comprised of Rho group and Cy group, it had the optical characteristic of rhodamine and Cy dyes. As shown in Figure S4A, the absorption peaks of Rho and Cy are 550 nm and 640 nm, respectively. However the absorption peaks of RhoSSCy in DMSO are 480 nm and 640 nm, respectively, as shown in Figure 1A. It means the conjugation of Rho group with Cy group resulted in blue shift of absorption peak of Rho group at 550 nm. In addition, the protonation and lower pH resulted in a red shift of the absorption peak from 640 nm to near infrared region (Figure S4B). As shown in Figure 1B, RhoSSCy has two emission peaks at 580 nm and 765 nm when excited at 480 nm. One of them came from Rho group and the other came from Cy group. Obviously. there was a good spectral overlap between the emission spectrum of the Rho (550-630 nm) and absorption spectrum of the Cy (580-700 nm), which resulted in the occurrence of fluorescence resonance energy transfer (FRET) from the excited state of Rho to Cy.

Fluorescence responses of RhoSSCy to glutathione (GSH) and pH *in vitro*

Firstly, RhoSSCy as a fluorescence probe showed dual-response to thiols and pH. As shown in Scheme 2, RhoSSCy on its original form could react with thiols (RSH) to form RhoSSR and HSCyH or react with H^+ to form RhoSSCyH$^+$. Meanwhile, it also could react with both H^+ and thiols at the same time to form RhoSSR and $HSCyH_2^+$. When RhoSSCy responded to thiols, the fluorescence emission intensity of probe at 580 nm (λ_{ex} = 480 nm) in the solution increased as the level of thiols increased (Figure 2A), which was because the disulfide bond of RhoSSCy could be splitted by reduced GSH and therefore the FRET effect disappeared. A GSH titration and calibration curve of RhoSSCy fluorescence intensity at 580 nm (λ_{ex} = 480 nm) was found to be directly proportional to the GSH concentration from 0.1 μM to 5 μM, and reached the upper plateau between 5 μM to 20 μM (Figure 2B and 2C).

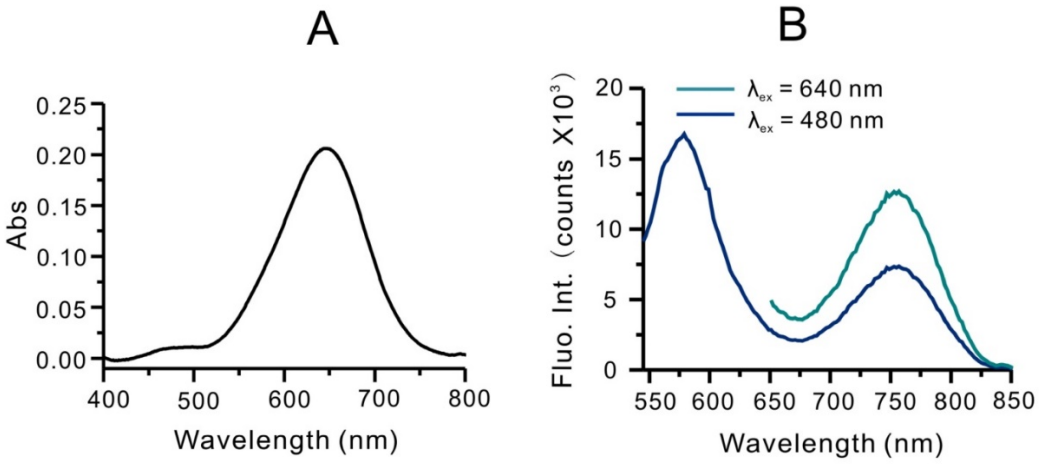

Figure 1. Optical properties of RhoSSCy. (A) UV-Vis absorption spectra of RhoSSCy in DMSO. (B) Fluorescence spectra of RhoSSCy in 20 mM PBS buffer (containing 1% DMF) upon excitation at 480 nm and 640 nm.

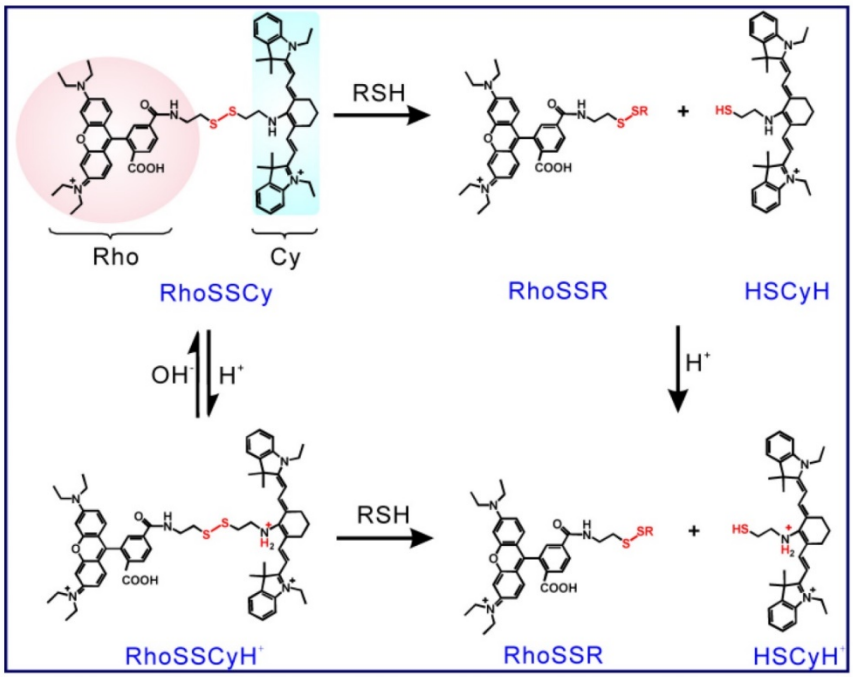

Scheme 2. The proposed response mechanisms of RhoSSCy to thiols and pH.

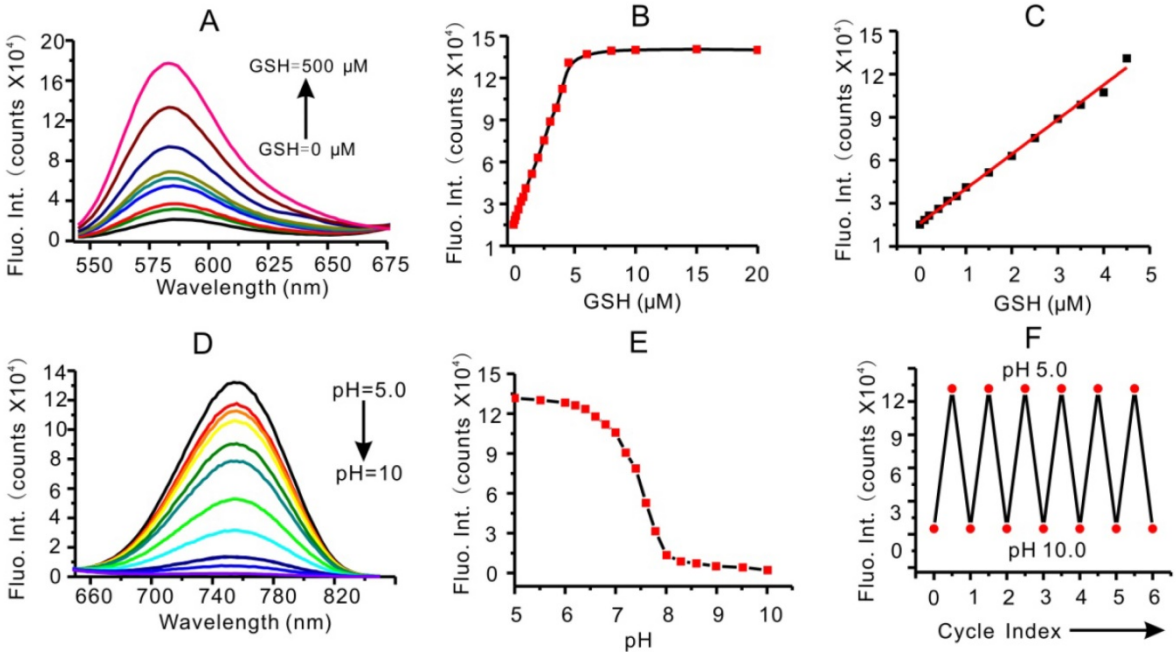

Figure 2. Fluorescence responses of RhoSSCy to biothiols and pH *in vitro*. (A) Emission spectra of RhoSSCy under increasing GSH levels (0, 1, 2, 3, 4, 5, 10, 50 and 500 μM). (B) Fluorescence-based GSH titration curve (λ_{ex} at 480 nm, λ_{em} at 580 nm). (C) The linear calibration plot of fluorescent intensity (λ_{ex} at 480 nm, λ_{em} at 580 nm) and its corresponding GSH concentration. (D) Emission spectra of RhoSSCy under decreasing pH value. (E) Fluorescence-based pH titration curve (λ_{ex} at 640 nm, λ_{em} at 765 nm). (F) The pH reversibility study of RhoSSCy between pH 5 and 10.

In fact, a drop of emission peak at 765 nm (λ_{ex} = 480 nm) was observed at the same time when GSH concentration increased and pH value remain unchanged (Figure S5A). So the ratio of fluorescent intensity at 765/580 nm was also directly proportional to the GSH concentration (Figure S5B and S5C). But in consideration of the interference of H^+ on fluorescence intensity at 765 nm, the above-mentioned ratiometric fluorescent detection could not be used alone in the complex system. It was necessary to take into account the fluorescent intensity of the probe at 580 nm at the same time. The calibration curves of fluorescence intensity at 580 nm versus GSH concentration were total overlapped at different pH values as shown in

Figure S5D. The fluorescence intensity at 580 nm was directly proportional to the GSH concentration regardless of the variation of pH value. Moreover, the selectivity of RhoSSCy to various RSH over intracellular species was investigated. The RhoSSCy showed good and uniform response to typical biothiols such as GSH, cysteine (Cys) and homocysteine (Hcy). However, when other amino acids and some possible coexisting organics were added to the solution of probe, the changes of RhoSSCy fluorescence intensity were negligible (Figure S5E).

RhoSSCy also has good response to pH in NIR region. As shown in Figure 2D, the fluorescent intensity of RhoSSCy at 765 nm (λ_{ex} = 640 nm) increased greatly as the pH value of probe solution decreased. RhoSSCy with the amino connected to Cy displayed 'switching on' of fluorescence upon protonation as the proton-induced suppression of photo-induced electron transfer (PET) led to fluorescence as the predominant deactivation pathway [57-59]. The pH titration curves illustrated that the fluorescence intensity of RhoSSCy at 765 nm was linearly related to pH values from pH 6.8 to 8.0 and the pKa value of probe was 7.4 (Figure 2E). The eppendorf tubes loaded with RhoSSCy solution at different pH values (pH 6.0, 6.4, 6.8, 7.2, 7.4) appeared obviously distinct in fluorescence image (Figure S3F). Most notably, the probe displayed an excellent stability and reversibility after 6 cycles between pH 5 and pH 9 (Figure 2F). Since the tumor microenvironment has low extracellular pH and at the same time our probe has good response to pH in NIR region [60], it is reasonable and feasible to use our probe to imaging tumor.

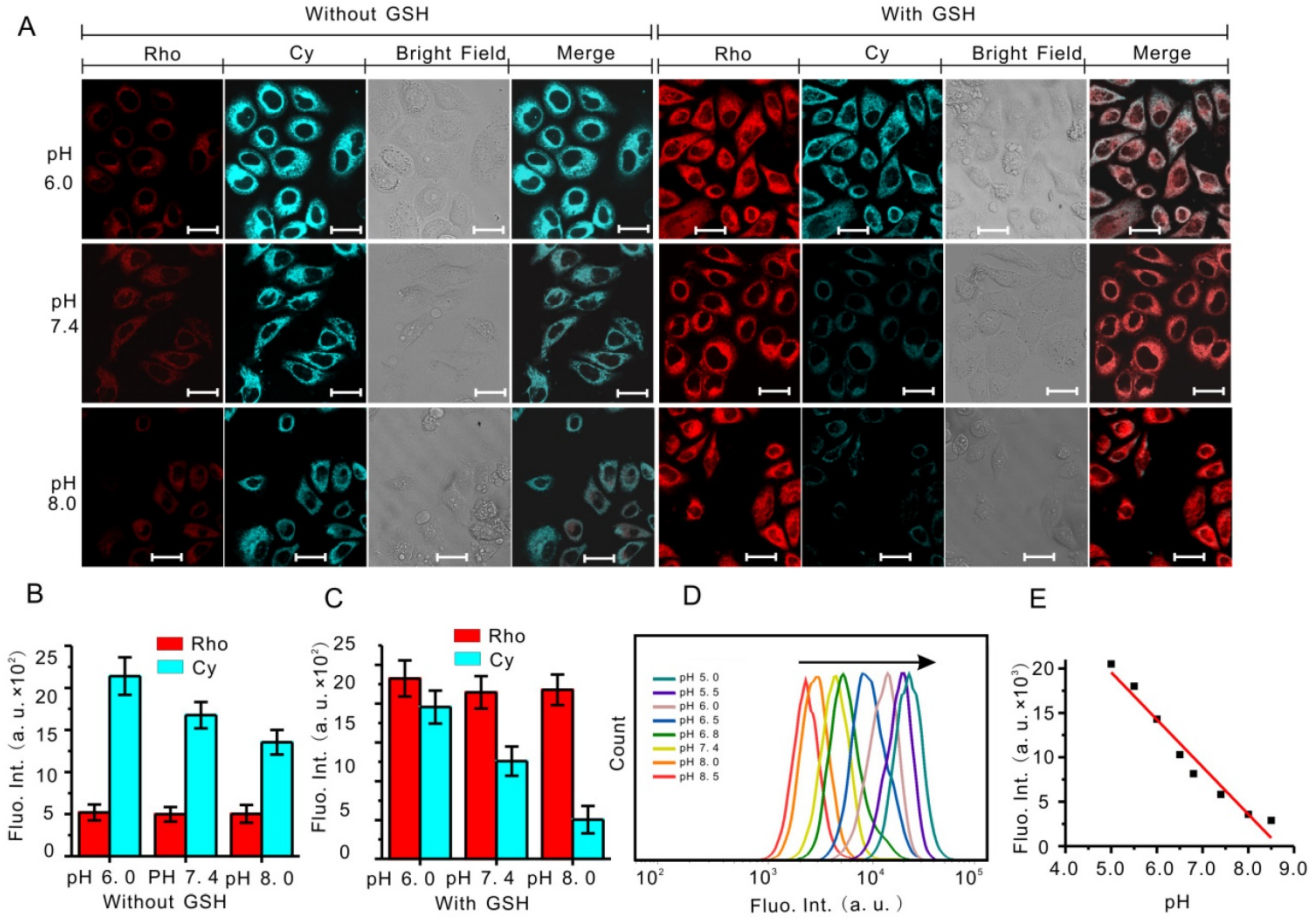

Figure 3. Fluorescence response of RhoSSCy to biothiols and pH in cells. (A) Fluorescent images of MCF-7 cells obtained in the presence and absence of GSH in buffer solution with different pH (6.0, 7.4 and 8.0). Bars, 25 μm. (B) Fluorescent intensity of the MCF-7 cells without GSH obtained from statistical analysis of the CLSM images in (A). (C) Fluorescent intensity of the MCF-7 cells with GSH obtained from statistical analysis of the CLSM images in (A). (D) Flow cytometry analysis of pH response of RhoSSCy to MCF-7 cells. (E) The linear calibration plot of fluorescent intensity and its corresponding pH value based on the flow cytometry analysis in (D).

The real-time imaging and monitoring of the cellular pH and GSH were performed by using confocal fluorescence imaging (CLSM). As shown in Figure 3A, MCF-7 cells without GSH incubated with RhoSSCy showed low red fluorescence at 550-620 nm (Rho channel), while cells with GSH showed strong fluorescence intensity at Rho channel. By contrast, the Cy fluorescence intensity at 660-800 nm (Cy channel) declined obviously with pH increasing. So in the merge channel obtained based on above two channels, the cells without GSH at pH 6.0 showed very weak red and very high Cy fluorescence, and on the contrary the cells with GSH at pH 8.0 showed strong red and low Cy fluorescence. The statistical results constructed according to these fluorescence images displayed a characteristic pH-dependent and thio-dependent signal change (Figure 3B and 3C), implying that RhoSSCy had excellent pH and biothiols dual-stimuli response to living cells *in vitro*.

Flow cytometric analysis is a reliable and convenient method for quantifying the cellular fluorescence intensity. To further confirm the pH response of RhoSSCy to cells, we applied flow cytometry to measure the cellular fluorescence variation in cells incubated with RhoSSCy under different pH. When the pH values were stepwisely reduced from 8.5 to 5.0, a gradual increase in fluorescence signal was observed (Figure 3D and Figure S6). Plotting this fluorescence change against each pH unit, we observed a total of ten folds fluorescence enhancement in every pH signal (Figure 3E), which further confirmed that the fluorescent intensity of RhoSSCy at 765 nm was highly correlated with pH value.

Targeting and accumulation of RhoSSCy in tumor cells

The Cy group in RhoSSCy has natively preferential tumor accumulation property [28]. In order to investigate the molecular targeting and accumulation ability of RhoSSCy in tumor cells, we compared the accumulation of RhoSSCy in tumorigenic and nontumorigenic cell models *in vitro*. After incubation cells with 10 μM RhoSSCy for 30 min, we tested the targeting and accumulation of RhoSSCy in normal cells and tumor cells by fluorescence confocal microscope and flow cytometry. The confocal fluorescence imaging from Figure 4A showed that the red fluorescence come from RhoSSCy was significantly higher in tumor cells (A549 cells and MCF-7 cells) than in normal cells (293-T cells), which indicated that RhoSSCy high-selectively accumulated in tumor cells. The results that the cellular uptake of RhoSSCy was also significantly higher in tumor cells than normal cells were also confirmed by flow cytometry (Figure 4B). The mechanism of RhoSSCy for tumor targeting is not clear, it is possibly associated with glycolytic metabolic patterns, which are preferentially utilized by tumor cells for energy supply, or organic-anion transporting polypeptide (OATP) transporters, which are well-recognized to be over-expressed in a variety of tumor cells [30, 61].

Dual-modal NIRF/PA imaging based on RhoSSCy

RhoSSCy is an ideal NIRF/PA dual-modality probe for tumor imaging and molecular tracing. The feasibility of *in vivo* tumor targeted NIRF/PA imaging with RhoSSCy was investigated by intravenous injection of RhoSSCy in subcutaneous MCF-7 tumor-bearing BALB/c nude mice. As shown in Figure 5A and 5B, the fluorescence signal firstly appeared in liver at 0.5 h postinjection, then the signal at the tumor site could be distinguished from the surrounding normal tissue at 10 h postinjection, and increased gradually to reach a maximum at 15 h postinjection. Thereafter, the signal at the tumor site began to drop, but was maintained even after 48 h postinjection, demonstrating that the tumor targeted delivery and long retention of RhoSSCy in tumor tissue.

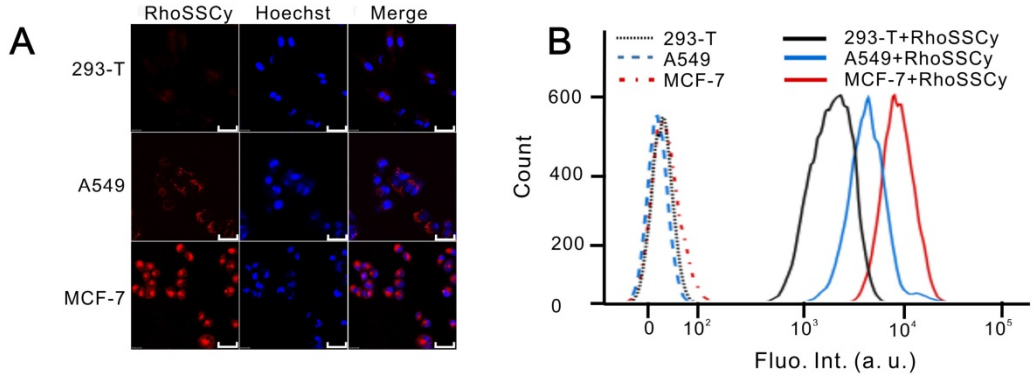

Figure 4. Cellular targeting and uptake of RhoSSCy. (A) Fluorescence confocal microscope images of normal cells (293-T cells) and tumor cells (A549 cells and MCF-7 cells) treated with RhoSSCy. Bars, 50 μm. (B) The accumulation of RhoSSCy in normal cells and tumor cells by using flow cytometry analysis.

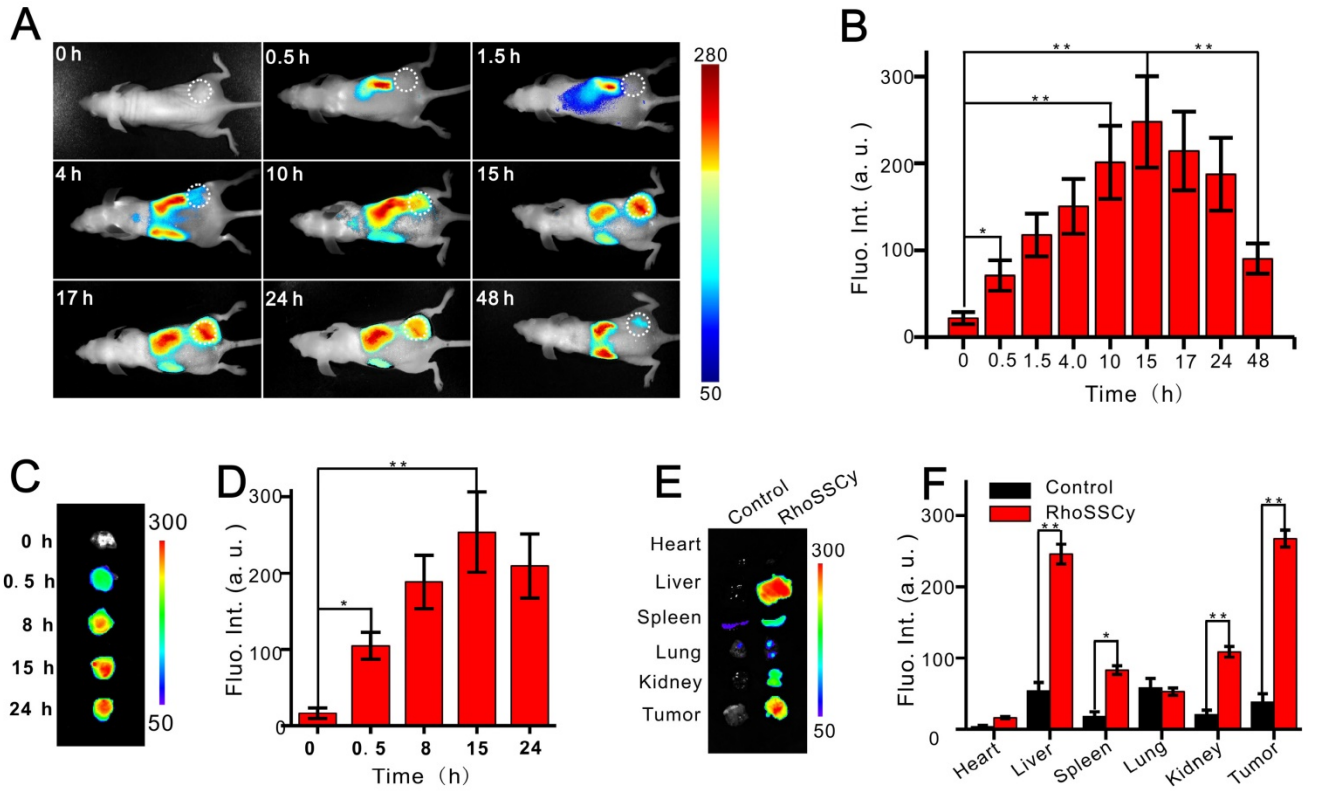

Figure 5. Tumor targeting NIRF imaging based on RhoSSCy. (A) NIRF imagings of tumor (white circle) in living mice at different time intervals after injection of RhoSSCy. (B) Semiquantitative fluorescent intensity (Fluo. Int.) of the tumor at indicated time-points. (C) *Ex vivo* NIRF imaging of dissected tumor tissue after tail vein injection of RhoSSCy. (D) Semiquantitative biodistribution of RhoSSCy in tumor determined by the averaged fluorescent intensity. (E) *Ex vivo* NIRF imaging of dissected tumor and organs come from mice in blank group (Control) and mice injected with RhoSSCy after 15 h postinjection. (F) Semiquantitative fluorescent intensity of dissected tumor and organs at indicated time-points. *P < 0.05, **P<0.01.

The *ex vivo* NIRF imaging of excised tumor tissue at different time points provided further evidence that RhoSSCy demonstrated excellent tumor targeted characteristic (Figure 5C and 5D). At 15 h postinjection, tumors and major organs were excised for *ex vivo* NIRF imaging to determine the tissue distribution of RhoSSCy. As shown in Figure 5E and 5F, the most RhoSSCy were accumulated in the liver and tumor tissue, and the spleen and kidneys showed relative weak fluorescence, while the fluorescence in the other regions of the mouse body was weaker compared with the fluorescence of RhoSSCy in tumor tissue. These results clearly indicated the RhoSSCy molecules preferentially accumulated in the tumor, which was in agreement with the tumor cells targeting *in vitro* mentioned above. After intravenous injection, fluorescence in some vital organs, such as liver, kidney, and spleen increased gradually. After 10 h, fluorescence in these organs decreased gradually (Figure 5A). The changes of the fluorescence signal indicated that RhoSSCy eliminated in hepatobiliary and renal excretion pathways from the animal body, which was similar with the metabolic pathway of other indocyanine dyes [62].

Photoacoustic imaging (PA) is a novel, hybrid, and noninvasive imaging modality that combines the merits of both optical and ultrasonic methods [63, 64], and also can evaluate the drug delivery efficiency and therapeutic effects with a relatively high spatial resolution in deep tissue. RhoSSCy has a strong NIR absorption band (between 650-700 nm) allowing deeper tissue penetration without causing significant heating. Thus it may be an ideal probe for PA imaging. As showing in Figure 6A, The PA signals of RhoSSCy in PBS solution increased with the increase of its concentrations under NIR laser illumination of 690 nm. Obviously, RhoSSCy could be a NIRF/PA dual-modality imaging probe with thiols and pH dual-responses.

We carried out *in vivo* PA imaging of nude mice bearing MCF-7 tumor injected with RhoSSCy by tail vein and measured the tumor signal before and various time points after injection. Figure 6B was the photo of nude mouse bearing MCF-7 tumor for PA imaging and white dash line indicated the position of PA imaging. Figure 6C showed the corresponding *ex vivo* cryoslice, which come from the software of whole body MSOT system and displayed the possible anatomic construction of the PA imaging in Figure 6D. Figure 6D and 6E indicated that the PA signals in

tumor tissue increased with time and distributed around with the tumor microvessels. The results suggested that the RhoSSCy molecules were greatly accumulated at tumor. The time-dependent curve of PA intensity showed that the PA signal in tumor tissue was clearly visible at 4h and reached maximum near 15 h post injection, which was in high agreement with the *in vivo* NIRF imaging behavior. It was clear that PA imaging provided a high spatial resolution, which was prone to understand the biodistribution of RhoSSCy in tumor tissue and got the delivery information on tumor microstructure.

Photodynamic therapy using RhoSSCy *in vitro* and *in vivo*

PDT has emerged as an effective treatment for tumor with minimal nonspecific damage to adjacent healthy tissues. It has been reported that some of the cyanine dyes have photosensitizing characteristics for cancer PDT [65, 66]. For instance, indocyanine green (ICG) has been extensively investigated as a potential photosensitizer by many research groups [67, 68]. The RhoSSCy has Cy group with potential photocytotoxic for PDT. We firstly detected reactive oxygen species (ROS) levels by RhoSSCy upon light irradiation. Intracellular ROS production was monitored by measuring the fluorescence intensity using DCF assay [69-71]. As shown in Figure 7A RhoSSCy can immediately produce ROS in the solution when 10 μM RhoSSCy solution was irradiated with 660 nm laser light at 30 mW/cm^2 power, and the ROS levels increased with the increase of RhoSSCy concentration. Furthermore, it seemed that the ROS levels produced by RhoSSCy were highly efficiency and even higher than chlorin e6 (Ce6) at the same concentration (Figure S7), which is a second-generation photosensitizer with high ROS yield. Therefore, the small-molecule probe RhoSSCy realizes multifunctions including thiols/pH sensing, NIRF/PA imaging and photoinduced ROS activity.

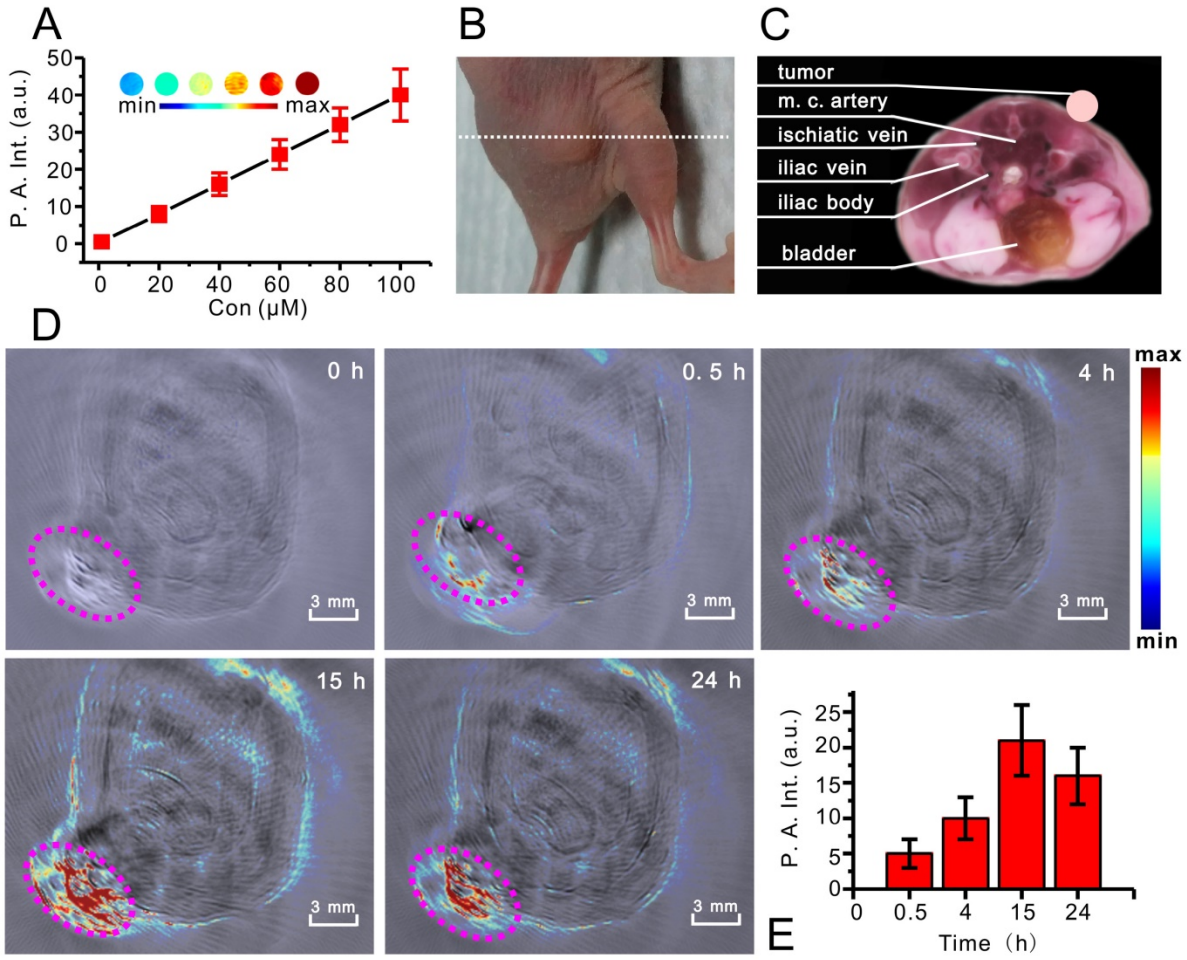

Figure 6. PA imaging based on RhoSSCy. (A) The linear relationship between PA intensity (P. A. Int.) and RhoSSCy concentration (Inset: PA images with different RhoSSCy concentrations). (B) The photo of nude mouse bearing MCF-7 tumor. White dash line indicated the position of PA imaging. (C) The corresponding *ex vivo* cryoslice of PA imaging, which come from the software of whole body MSOT system. (D) PA imaging of a tumor bearing nude mouse. Pink circle indicated the location of tumor. (E) Semiquantitative fluorescent intensity of the tumor at indicated time points.

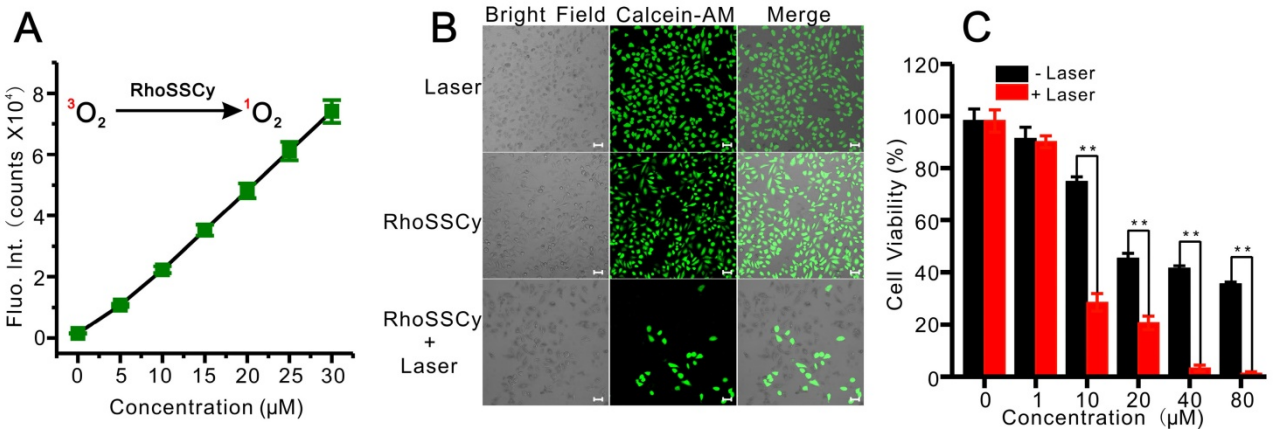

Figure 7. Photodynamic therapy using RhoSSCy *in vitro*. (A) The linear relationship between fluorescent intensity of DCF, which correlated to the release of ROS, and RhoSSCy concentration. (B) Fluorescent images of MCF-7 cells under the different conditions. Viable cells were stained green with calcein-AM. Bars, 25 μm. (C) Cell survivals of MCF-7 after PDT treatment using RhoSSCy with different concentration.

To study the photodynamic efficacy of RhoSSCy *in vitro*, the PDT-induced cell death was examined through measuring fluorescence of calcein-AM, which stained viable cells green and dead cells show no fluorescence. After MCF-7 cells were incubated with 10 μM RhoSSCy for 4 h and followed by NIR laser irradiation (660 nm, 30 mW/cm^2) for 5 min, the cells were stained with calcein-AM. As shown in Figure 7B, most of the cells treated with RhoSSCy plus laser irradiation were colorless, indicating apparent cell death after 24 h, while the cells treated with RhoSSCy only and the cells treated with laser irradiation only were almost entirely alive. These results suggested the cytotoxicity of RhoSSCy mainly came from PDT effect. Cytotoxicity assay shown in Figure 7C demonstrated that RhoSSCy group without laser irradiation was only affected cell viability at high concentration (>10 μM). The dark cytotoxicity is presumably ascribed to the water-insolubility and specific chemical structure of RhoSSCy. On the other hand, the laser-radiated groups exhibited more obvious PDT induced cytotoxicity with the increase of the concentration of RhoSSCy (Figure 7C).

On the basis of the excellent NIRF/PA dual-modal imaging response *in vivo* and the high efficient PDT of RhoSSCy *in vitro*, we further applied RhoSSCy for imaging-guided tumor phototherapy *in vivo*. RhoSSCy was intravenously injected into tumor-bearing mice when the tumor size grew to 50-100 mm^3. At 15 h after injection, which was the time when the accumulation of RhoSSCy in tumor reached the maximum as previously confirmed with NIFR/PA imaging, mice were irradiated at the tumor site with a safe NIR laser (660 nm, 100 mW/cm^2) for 30 min. *In vivo* therapeutic efficacy of RhoSSCy was evaluated by the growth rate of relative volume of tumors (Figure 8A). Compared with other groups, the mice treated with RhoSSCy plus laser irradiation showed remarkable tumor growth suppression and valuable tumor regression after two weeks. In contrast, RhoSSCy-treated mice without laser irradiation showed no apparent change of tumor size which indicated that the therapeutic effect was highly depended on light-triggering PDT. Hence, it was noteworthy that RhoSSCy exhibited robust PDT therapeutic efficacy.

Moreover, the survive rate of RhoSSCy-treated mice with laser irradiation was also extensively improved to 80%, while saline-treated mice with laser is only 10% (Figure 8B). During the treatments, the body weight was monitored, which suggested the treatments-induced toxicity (Figure 8C). The weight of the groups treated with saline and saline plus laser irradiation gradually increased 16% and 15% on day 30, and RhoSSCy-treated mice with or without laser irradiation increased their body weights respectively by 15.7% and 14.1%. The body weight of these experimental groups was not significantly different from the control group, indicating that those treatments were reasonably well-tolerated. As shown in Figure 8D, no noticeable abnormality was observed from the H&E-stained organ slices of major organs including liver, spleen, kidney, heart, and lung come from the PDT-treated mice, suggesting the negligible toxic side effects of RhoSSCy for PDT *in vivo*. However, prominent necrosis was observed in the PDT-treated tumor tissue, while necrosis was indiscernible in the non-irradiated tumor in H&E-stained tumor slices. The results above clearly demonstrated that tumor-targeted photodynamic therapy of RhoSSCy was highly effective and safe *in vivo*.

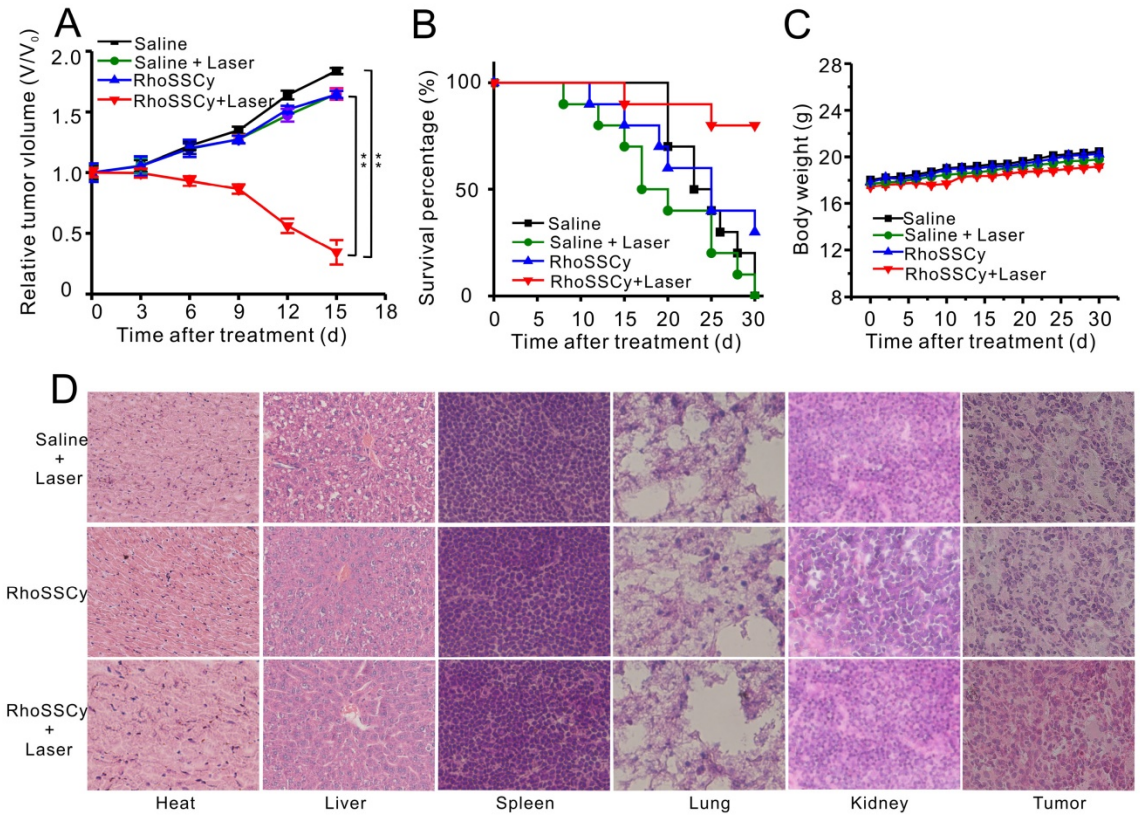

Figure 8. *In vivo* PDT therapy using RhoSSCy. (A) The growth curve of MCF-7 xenograft tumors within 15 days in different groups (n = 6). *p < 0.05, **p < 0.01. (B) Survival rate of mice bearing MCF-7 tumors of disparate groups within 30 d after corresponding treatments. (C) Body weight change of mice under different conditions. (D) H&E stained images of sliced major organs and tumors collected from different groups.

Discussion and Conclusions

We developed a new near infrared multifunctional small-molecule theranostic probe RhoSSCy, which exhibited dual-responsive to both thiols and pH, intrinsic preferential tumor accumulation, NIRF/PA dual-modal imaging, and NIR-sensitizing PDT activities. Biothiols and acid-base equilibrium play critical roles in biological processes, so it is necessary to develop efficient methods to monitor biothiols and pH level in living cells. When two or more molecules need to be examined in a system at the same time, a general method is to use two different probes simultaneously. However, this strategy often suffers from uneven probes loading, nonhomogeneous distribution, uncontrollable localization, larger invasive effects, metabolisms, and spectral overlap interference between probes. Compared with the single response probes, the dual-response probes which can selectively respond to dual-species should be more appropriate for visualizing variation of objects under test for biological events. To the best of our knowledge, a small-molecule probe that could display differential fluorescence OFF-ON dual-response to thiols and pH simultaneously has not been covered in the literature.

Additionally, RhoSSCy probe had the ability to high-selectively accumulate into the tumor cells and tissue. Moreover, the solid tumor microenvironment is generally acidic and the fluorescence of RhoSSCy probe was enhanced in the near infrared region under the acidic condition. So it was suitable for tumor fluorescence imaging. At the same time, RhoSSCy had a strong absorption band (650-700 nm) allowing deeper tissue penetration without causing significant heating and so it was also appropriate for PA imaging. Traditional imaging techniques are frequently limited by narrow penetration, low sensitivity, low specificity, and poor spatial resolution. RhoSSCy as a dual-modal NIR/PA molecular imaging probe had a great potentiality to exceed most of these limitations.

Moreover, RhoSSCy as a robust photosensitizer was applied for PDT treatment in a subcutaneous carcinoma model. After the laser-triggered PDT treatment, the tumor size was highly suppressed and the mice survival was greatly promoted. The superiority of tumor targeting dual-modal imaging and PDT treatment was integrated into a small-molecule probe of RhoSSCy, which could provide the complementary information for accurate imaging-diagnosis, imaging-guided phototherapy

and curative effect assessment of tumor. These results highlighted the potential of RhoSSCy as a versatile theranostic agent to tumor targeted sensing and imaging-guided PDT.

In summary, we reported a first small-molecule probe RhoSSCy with "Four in One" mutifunctions for sensing, targeting, multi-modal imaging and therapy. RhoSSCy probe was synthesized by conjugating Rho with Cy using a disulfide linker and a pH tunable amino-group, which resulted in ratiometric detection of free thiols and directly sensing intracellular change of pH and thiol concentration together. Meanwhile, RhoSSCy molecules entered tumor cells easily and preferentially accumulated in the tumor. Furthermore, it simultaneously displayed NIRF/PA dual-modal imaging capability and efficient PDT anticancer effect *in vitro* and *in vivo*. With great efforts in overcoming the drawbacks of NIR dyes and integrating fantastic theranostics, there is no doubt that this well-defined small-molecule probe RhoSSCy was valuable not only to multi-modality imaging application, but also to target-specific molecular diagnosis and phototherapy treatment of cancers.

Supplementary Material

Supplementary figures and tables.
http://www.thno.org/v07p1781s1.pdf

Acknowledgment

This work was supported by the National Natural Science Foundation of China (21375141, 81671758, 31571013, 51502333, 81401509, 21404115 and 81501580), Key International S&T Cooperation Project (2015DFH50230), Instrument Developing Project of CAS (YZ201439), Guangdong Natural Science Foundation of Research Team (2016A030312006), Shenzhen Science and Technology Program (JSGG20160331185422390, JCYJ20150403091443298, KQCX20140521115045447, JCYJ20160429191503002).

Competing Interests

The authors have declared that no competing interest exists.

References

1. Jeelani S, Reddy RC, Maheswaran T, et al. Theranostics: A treasured tailor for tomorrow. J Pharm Bioallied Sci. 2014; 6(Suppl 1): S6-S8.
2. Bardhan R, Lal S, Joshi A, et al. Theranostic nanoshells: from probe design to imaging and treatment of cancer. Acc Chem Res. 2011; 44(1): 936-946.
3. Sumer B, Gao J. Theranostic nanomedicine for cancer. Nanomedicine. 2008; 3(2): 137-140.
4. Fan Z, Fu PP, Yu H, et al. Theranostic nanomedicine for cancer detection and treatment. J Food Drug Anal. 2014; 22(1): 3-17.
5. Sharma R, Mody N, Agrawal U, et al. Theranostic nanomedicine; a next generation platform for cancer diagnosis and therapy. Mini Rev Med Chem. 2016; 16(999): 1.
6. Muthu MS, Agrawal P, Singh S. Theranostic nanomedicine of gold nanoclusters: an emerging platform for cancer diagnosis and therapy. Nanomedicine. 2016; 11(4): 327-330.
7. Mccarthy JR. The future of theranostic nanoagents. Nanomedicine. 2009; 4(7): 693-5.
8. Wang LN, Wang YB, Li ZJ. Nanoparticle-based tumor theranostics with molecular imaging. Curr Pharm Biotechno. 2013; 14(7): 683-692.
9. Bao CC, Conde J, Pan F, et al. Gold nanoprisms as a hybrid in vivo cancer theranostic platform for in situ photoacoustic imaging, angiography, and localized hyperthermia. Nano Res. 2016; 9(4): 1043-1056.
10. Brannon-Peppas L, Blanchette JO. Nanoparticle and targeted systems for cancer therapy. Adv Drug Deliv Rev. 2012; 56(11): 1649-1659.
11. Park K, Lee S, Kang E, et al. New generation of multifunctional nanoparticles for cancer imaging and therapy. Adv Funct Mater. 2009; 19(10): 1553-1566.
12. Cai W, Chu CC, Liu G, et al. Metal-organic framework-based nanomedicine platforms for drug delivery and molecular imaging. Small. 2015; 11(37): 4806-4822.
13. Chow EK, Ho D. Cancer nanomedicine: from drug delivery to imaging. Sci Transl Med. 2013; 5(216): 1039-1048.
14. Doane TL, Burda C. The unique role of nanoparticles in nanomedicine: imaging, drug delivery and therapy. Chem Soc Rev. 2012; 41(27): 2885-2911.
15. Khemtong C, Kessinger CW, Gao J. Polymeric nanomedicine for cancer MR imaging and drug delivery. Chem Commun. 2009; 24(41): 3497-3510.
16. Liu Y, Miyoshi H, Nakamura M. Nanomedicine for drug delivery and imaging: a promising avenue for cancer therapy and diagnosis using targeted functional nanoparticles. Int J Cancer. 2007; 120(12): 2527-2537.
17. Wang J, Wang F, Li F, et al. A multifunctional poly(curcumin) nanomedicine for dual-modal targeted delivery, intracellular responsive release, dual-drug treatment and imaging of multidrug resistant cancer cells. J Mater Chem B. 2016; 4(17): 2954-2962.
18. Luo S, Zhang E, Su Y, et al. A review of NIR dyes in cancer targeting and imaging. Biomaterials. 2011; 32(29): 7127-7138.
19. Lim EK, Kim T, Paik S, et al. Nanomaterials for theranostics: recent advances and future challenges. Chem Rev. 2014; 115(1): 327-394.
20. Wang YXJ, Idee JM, Corot C. Scientific and industrial challenges of developing nanoparticle-based theranostics and multiple-modality contrast agents for clinical application. Nanoscale. 2015; 7(39): 16146-16150.
21. Yang K, Hu L, Ma X, et al. Multimodal imaging guided photothermal therapy using functionalized graphene nanosheets anchored with magnetic nanoparticles. Adv Mater. 2012; 24(14): 1868-1872.
22. Wang C, Cheng L, Liu YM, et al. Imaging-guided pH-sensitive photodynamic therapy using charge reversible upconversion nanoparticles under near-infrared light. Adv Funct Mater 2013; 23(24): 3077-3086.
23. Setyawati MI, Tay CY, Docter D, et al. Understanding and exploiting nanoparticles' intimacy with the blood vessel and blood. Chem Soc Rev. 2015; 44(22): 8174-8199.
24. Nel A, Xia T, Madler L, et al. Toxic potential of materials at the nanolevel. Science. 2006; 311(5761): 622-7.
25. Hoshino A, Hanada S, Yamamoto K. Toxicity of nanocrystal quantum dots: the relevance of surface modifications. Arch Toxicol. 2011; 85(7): 707-720.
26. Kim T, Huh YM, Haam S, et al. Activatable nanomaterials at the forefront of biomedical sciences. J Mater Chem. 2010; 20(38): 8194-8206.
27. Wilhelm S, Tavares AJ, Dai Q, et al. Analysis of nanoparticle delivery to tumours. Nat Rev Mater. 2016; 1(5): 16014.
28. Luo SL, Zhang EL, Su YP, et al. A review of NIR dyes in cancer targeting and imaging. Biomaterials. 2011; 32(29): 7127-7138.
29. Aulic S, Bolognesi ML, Legname G. Small-molecule theranostic probes: a promising future in neurodegenerative diseases. Int J Cell Biol. 2013; 2013(5012): 150952.
30. Zhang EL, Luo SL, Tan X, et al. Mechanistic study of IR-780 dye as a potential tumor targeting and drug delivery agent. Biomaterials. 2013; 35(2): 771-8.
31. Luo SL, Tan X, Qi QR, et al. A multifunctional heptamethine near-infrared dye for cancer theranosis. Biomaterials. 2013; 34(9): 2244-2251
32. Xing, R., Liu, K., Jiao, T., et al. An injectable self-assembling collagen–gold hybrid hydrogel for combinatorial antitumor photothermal/photodynamic therapy. Adv Mater. 2016; 28(19): 3669–3676.
33. Owens EA, Lee S, Choi J, et al. NIR fluorescent small molecules for intraoperative imaging. Wires Nanomed Nanobi. 2015; 7(6): 70-83
34. Wu JB, Lin TP, Gallagher JD, et al. Monoamine oxidase a inhibitor-near-infrared dye conjugate reduces prostate tumor growth. J Am Chem Soc. 2015; 137(6): 2366-2374.
35. Tan X, Luo S, Wang D, et al. A NIR heptamethine dye with intrinsic cancer targeting, imaging and photosensitizing properties. Biomaterials. 2012; 33(7): 2230-2239.
36. Zhang C, Liu T, Su YP, et al. A near-infrared fluorescent heptamethine indocyanine dye with preferential tumor accumulation for in vivo imaging. Biomaterials. 2010; 31(25): 6612-6617.
37. Luo SL, Tan X, Qi QR, et al. A multifunctional heptamethine near-infrared dye for cancer theranosis. Biomaterials. 2013; 34(9): 2244-2251.
38. Wada H, Hyun H, Vargas C, et al. Pancreas-Targeted NIR Fluorophores for Dual-Channel Image-Guided Abdominal Surgery. Theranostics. 2015; 5(1): 1-11.
39. Njiojob CN, Owens EA, Narayana L, et al. Tailored near-infrared contrast agents for image guided surgery. J Med Chem. 2015; 58(6): 2845-2854.
40. Hyun H, Park MH, Owens EA, et al. Structure-inherent targeting of near-infrared fluorophores for parathyroid and thyroid gland imaging. Nat Med. 2015; 21(2): 192-197.

41. Wood ZA, Schroder E, Robin HJ, et al. Structure, mechanism and regulation of peroxiredoxins. Trends Biochem Sci. 2003; 28(1): 32-40.
42. Herzenberg LA, Rosa SCD, Dubs JG, et al. Glutathione deficiency is associated with impaired survival in HIV disease. Proc Natl Acad Sci USA. 1997; 94(5): 1967-1972.
43. Jacobsen DW. Homocysteine and vitamins in cardiovascular disease. Clin Chem. 1998; 44(2): 1833-1843.
44. Shahrokhian SL. Phthalocyanine as a selective carrier for preparation of a cysteine-selective electrode. Anal Chem. 2001; 73(24): 5972-5978.
45. Townsend DM, Tew KD, Tapiero HB. The importance of glutathione in human disease. Pharmacother. 2003; 57(3-4): 145-155.
46. Meade TJ, Aime S. Chemistry of molecular imaging. Acc Chem Res. 2009; 42(7): 821.
47. Ueno T, Nagano T. Fluorescent probes for sensing and imaging. Nat Methods. 2011; 8(8): 642-645.
48. Pittet MJ, Weissleder R. Fluorescent probes for sensing and imaging. Cell. 2011; 147(5): 983-991.
49. James ML, Gambhir SS. A molecular imaging primer: modalities, imaging agents, and applications. Physiol Rev. 2012; 92(2): 897-965.
50. Chang PV, Bertozzi CR. Imaging beyond the proteome. Chem Commun. 2012; 48(71): 8864-8879.
51. Toullec A, Gerald D, Despouy G, et al. Oxidative stress promotes myofibroblast differentiation and tumour spreading. EMBO Mol Med. 2010; 2(6): 211–230.
52. Fiasch T, Chiarugi P. Oxidative stress, tumor microenvironment, and metabolic reprogramming: a diabolic liaison. Int. J. Cell Biol. 2012; 2012(1): 762825.
53. Dirican N, Dirican A, Sen O, et al. Thiol/disulfide homeostasis: a prognostic biomarker for patients with advanced non-small cell lung cancer. Redox Rep. 2016; 21(5): 197-203.
54. Lou Z, Li P, Song P, et al. Ratiometric fluorescence imaging of cellular hypochlorous acid based on heptamethine cyanine dyes. Analyst. 2013; 138(21): 6291-6295.
55. Yuan L, Lin W, Xie Y, et al. Fluorescent detection of hypochlorous acid fromturn-on to fret-based ratiometry by a hocl-mediated cyclization reaction. Chem-Eur J. 2012; 18(9): 2700-2706.
56. Tafani M, Cohn JA, Karpinich NO, et al. Regulation of intracellular pH mediates Bax activation in HeLa cells treated with staurosporine or tumor necrosis factor-alpha. J Biol Chem. 2002; 277(51): 49569-49576.
57. Ma Z, Lin YX, Chen H, et al. A novel NBD-based pH "on–off" fluorescent probe equipped with the N-phenylpiperazine group for lysosome imaging. Rsc Adv. 2016; 6: 102773-102777
58. Rice TE, Silva APD, Gunaratne HQN, et al. Regiocontrol of fluorescent PET (photoinduced electron transfer) pH sensors. Proc SPIE. Adv Fluoresc Sens Tech II, 1995; 2388: 257-264.
59. Bryan AJ, Silva APD, Silva SAD, et al. Photoinduced electron-transfer as a general design logic for fluorescent molecular sensors for cations. Biosensors, 1989; 4: 169-179.
60. Prescott DM, Charles HC, Poulson JM, et al. The relationship between intracellular and extracellular pH in spontaneous canine tumors. Clin Cancer Res. 2000; 6(6): 2501-2505.
61. Luo S, Tan X, Fang S, et al. Mitochondria-targeted small-molecule fluorophores for dual modal cancer phototherapy. Adv Funct Mater. 2016; 26(17): 2826-2835.
62. Monfared A, Blevins NH, Cheung EL, et al. In vivo imaging of mammalian cochlear blood flow using fluorescence microendoscopy. Ontol Neurotol. 2006; 27(2): 144-152.
63. Yang X, Wang LV. Photoacoustic tomography of a rat cerebral cortex with a ring-based ultrasonic virtual point detector. J Biomed Opt. 2007; 12(12): 769-775.
64. Yang X, Skrabalak SE, Li ZY, et al. Photoacoustic tomography of a rat cerebral cortex in vivo with au nanocages as an optical contrast agent. Nano Lett. 2007; 7(12): 3798-3802.
65. Delaey E, Van LF, De VD, et al. A comparative study of the photosensitizing characteristics of some cyanine dyes. J Photoch Photobio B. 2000; 55(1): 27-36.
66. Kulbacka J, Pola A, Mosiadz D, et al. Cyanines as efficient photosensitizers in photodynamic reaction: photophysical properties and in vitro photodynamic activity. Biochemistry(Moscow). 2011; 76(4): 473-9.
67. Sheng Z, Hu D, Zheng M, et al. Smart human serum albumin-indocyanine green nanoparticles generated by programmed assembly for dual-modal imaging-guided cancer synergistic phototherapy. ACS Nano. 2014; 8(12): 12310-12322.
68. Sheng ZH, Hu DH, Xue MM, et al. Indocyanine green nanoparticles for theranostic applications. Nano-Micro Lett. 2013; 5(3): 145-150.
69. Xue Q, Wang P, Wang X, et al. Targeted inhibition of p38MAPK-enhanced autophagy in SW620 cells resistant to photodynamic therapy-induced apoptosis. Lasers Med Sci. 2015; 30(7): 1967-1975.
70. Yang M, Jalloh AS, Wei W, et al. Biocompatible click chemistry enabled compartment-specific pH measurement inside E. coli, Nat. Commun. 2014; 5: 4981-4990.
71. Yuan Y, Feng G, Qin W, et al. Targeted and image-guided photodynamic cancer therapy based on organic nanoparticles with aggregation-induced emission characteristics, Chem. Commun. (Camb) 2014; 50 (63):8757-8760.